CuFeS$_2$ Quantum Dots and Highly Luminescent CuFeS$_2$ Based Core/Shell Structures: Synthesis, Tunability, and Photophysics

Biswajit Bhattacharyya and Anshu Pandey*

Solid State and Structural Chemistry Unit, Indian Institute of Science, Bangalore 560012, India

S *Supporting Information*

ABSTRACT: We report the synthesis of copper iron sulfide (CuFeS$_2$) quantum dots (QDs). These materials exhibit a tunable band gap that spans the range 0.5−2 eV (600−2500 nm). Although the as-prepared material is nonemissive, CuFeS$_2$/CdS core/shell structures are shown to exhibit quantum yields that exceed 80%. Like other members of the I−III−VI$_2$ family QDs, CuFeS$_2$ based nanoparticles exhibit a long-lived emission that is significantly red-shifted compared to the band gap. CuFeS$_2$ QDs are unique in terms of their composition. In particular, these QDs are the only band-gap-tunable infrared chromophore composed entirely of elements with atomic numbers less than 30.
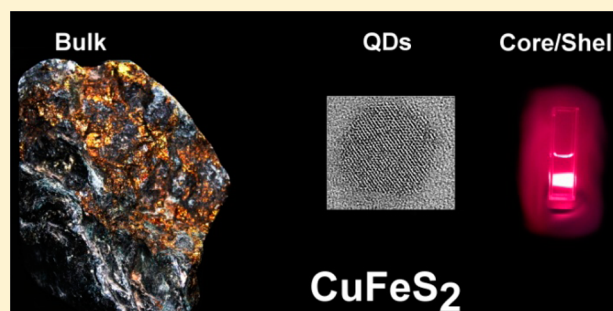
INTRODUCTION

The ever-increasing interest in cheap, efficient, solution processable photovoltaics[1] has inspired considerable research into the development of infrared semiconductor materials. Besides their importance for photovoltaics,[2] infrared semiconductor quantum dots (QDs) are useful in a range of other applications, including photodetection[3] and fluorescence labeling.[4] Most infrared semiconductor QDs that have band gaps tunable in the 0.5−1.5 eV region are composed of heavier elements. Examples include PbSe,[5−7] CdTe,[8−12] SnTe,[13,14] InSb,[15,16] HgTe,[17−19] CuInSe$_2$,[20−23] Ge,[24,25] and Ag$_2$Se.[26,27] QDs composed of Cu$_2$S[28−30] and FeS$_2$[31,32] exhibit only a limited band gap tunability. The involvement of heavier elements such as lead,[33] cadmium,[34] and tin[33] in near-infrared semiconductors limits their large-scale usage because of both economic and environmental considerations. Even a seemingly innocuous metal such as tin[33,35] has been found to be extremely toxic and hazardous in its divalent state.

Here we report a synthesis of copper iron sulfide QDs. CuFeS$_2$ is a naturally occurring mineral with a distinctive golden luster. It usually occurs in a tetragonal chalcopyrite structure. Although its abundance suggests its stability under terrestrial conditions, CuFeS$_2$ remains difficult to synthesize in a laboratory setting. In particular, there have been no previous reports of size tunability or luminescence of CuFeS$_2$ based QDs.

As a semiconductor, CuFeS$_2$ is reported to have a bulk band gap in the region of 0.5−0.6 eV.[36,37] CuFeS$_2$ is rather unique even among the copper ternaries because of the partial (+II) oxidation state character of the copper centers. Besides its obviously useful band gap,[38] CuFeS$_2$ plays host to several other physical phenomena such as thermoelectricity[39] and ferroelectricity.[40,41] The exploration of its unusual physical properties however remains stymied by the lack of a stable synthetic route to CuFeS$_2$ QDs and core/shells.

SYNTHESIS

We synthesized CuFeS$_2$ QDs as well as core/shell structures through a colloidal chemical route, and analyzed their structural, optical, and electronic properties.

In a typical synthesis, Cu(CH$_3$COO)$_2$ and FeCl$_2$ were taken in a round bottomed flask. 1-Octadecene (ODE, 2 mL) was employed as a solvent, while oleic acid (2 mL) was used as a ligand. The reaction mixture is first heated to 100 °C under vacuum for 5 min. The reaction mixture is then heated to 120 °C under argon for 10 min. At this stage, the metal precursors are observed to dissolve in the reaction mixture, imparting a brownish color. A 1.5 mL volume of dodecanethiol (DDT) is now injected into the flask and the contents are heated to 180 °C to initiate the nucleation of CuFeS$_2$ QDs. Within a few seconds of this heating step, the contents of the flask turn from brown to pale yellow in color. Sulfur in oleyl amine (see the Supporting Information for preparation details) is now injected dropwise (0.1 mL/min) to this solution. The growth solution darkens rapidly upon the addition of the sulfur precursors. These color changes are associated with the appearance of CuFeS$_2$ QDs. These QDs exhibit typical signs of quantum confinement such as a tunable band gap. Through this synthetic route, it is possible to prepare QDs that exhibit absorption edges ranging from 2 eV to about 0.5 eV (bulk band gap of CuFeS$_2$),[36] thereby sampling strong, intermediate, and weak confinement regimes of this material (see Figure 1a). The as-prepared CuFeS$_2$ QDs have a tetragonal chalcopyrite structure. This is exemplified in Figure 1b. The excellent agreement of the
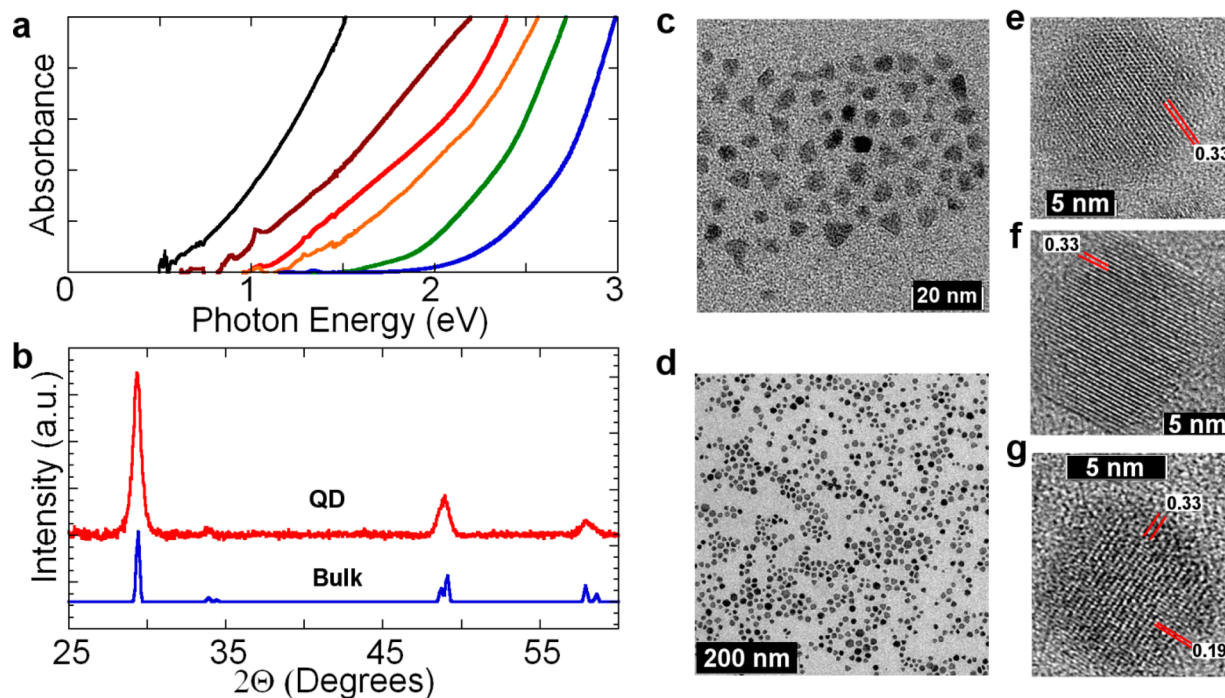
Figure 1. (a) Tunable absorbance of $CuFeS_2$ QDs. (b) XRD pattern of $CuFeS_2$. (c, d) TEM images of $CuFeS_2$ QDs. (e−g) HRTEM images of $CuFeS_2$ QDs showing lattice fringes. The red lines indicate interplanar spacings. A 0.33 nm spacing corresponds to the (112) plane of a tetragonal chalcopyrite structure, while a 0.19 nm spacing corresponds to the (204) plane.

pattern exhibited by QDs (red, top) with the bulk patterns (blue, bottom) as well as the absence of secondary phases is indicative of a high structural purity of these materials. Transmission electron micrographs (TEM) of these particles suggest a monodisperse ensemble with an 11.9% size distribution (Figure 1c,d). High resolution TEM (HRTEM) shows the presence of high quality single crystalline QDs with a chalcopyrite phase, as observed in X-ray diffraction (XRD; Figure 1e−g). Interplanar spacings of 0.33 and 0.19 nm are observed, corresponding to the (112) and (204) planes.

The synthetic route adopted by us requires the complete initial dissolution of iron and copper precursors prior to addition of the thiol. Addition of thiol to incompletely solubilized metal precursors is found to lead to nucleation of undesirable phases corresponding to iron and copper sulfides. Further, the slow sulfur injection allows for a very precise control of the QD band gap. Figure 2a shows the evolution of the band gap during a typical synthesis. Progressive growth leads to a shift of the sample band gap to around 0.5 eV over 12 min (Figure 2a, red diamonds). This shift of the band gap is accompanied by a simultaneous narrowing of the diffraction lines corresponding to various chalcopyrite reflections. Figure 2a shows that the reflection corresponding to the (112) plane (blue circles) narrows to 0.5°, indicating a corresponding increase in crystallite size. The corresponding patterns are shown in the inset. We further note that no secondary phases are observed at any stage, suggesting a relatively straightforward nucleation and growth picture for the formation of these QDs under the above-mentioned reaction conditions.

Our synthetic method also emphasizes lower growth temperatures as opposed to other $CuFeS_2$ nanoparticle preparation schemes reported in the literature. We note that the use of high temperatures (>200 °C) leads to a very rapid nanoparticle growth, and consequently the resulting particles do not exhibit size tunability or quantum confinement. In
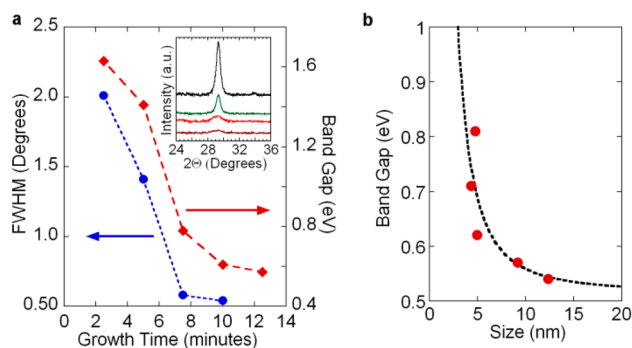

Figure 2. (a) Variation of full width at half-maximum (fwhm) of the (112) reflection (blue circles) and band gap (red diamonds) as a function of growth time. (b) Variation of band gap with QD size. The data fit to a bulk band gap of 0.52 eV and a reduced excitonic mass of 0.35.

contrast, the lower reaction temperature (180 °C) adopted by us leads to a slower increase in particle size, allowing us to synthesize precisely controlled size tunable quantum confined QDs.

■ EFFECTIVE MASS

We studied the shift of the band gap as a function of $CuFeS_2$ QD size (Figure 2b). In Figure 2b, the QD sizes have been determined through TEM imaging. The y axis shows the absorption onset (optical band gap) of these materials. In each case, the optical gap is determined from a Tauc plot (e.g., Figure S1). The band gap is seen to vary as $\frac{1}{size^2}$, consistent with a spherical particle in a box. Taking the conduction and valence band envelop functions of this system to be S-like, it is possible to extract the excitonic reduced mass of this system. We find that this material exhibits a rather high excitonic reduced mass
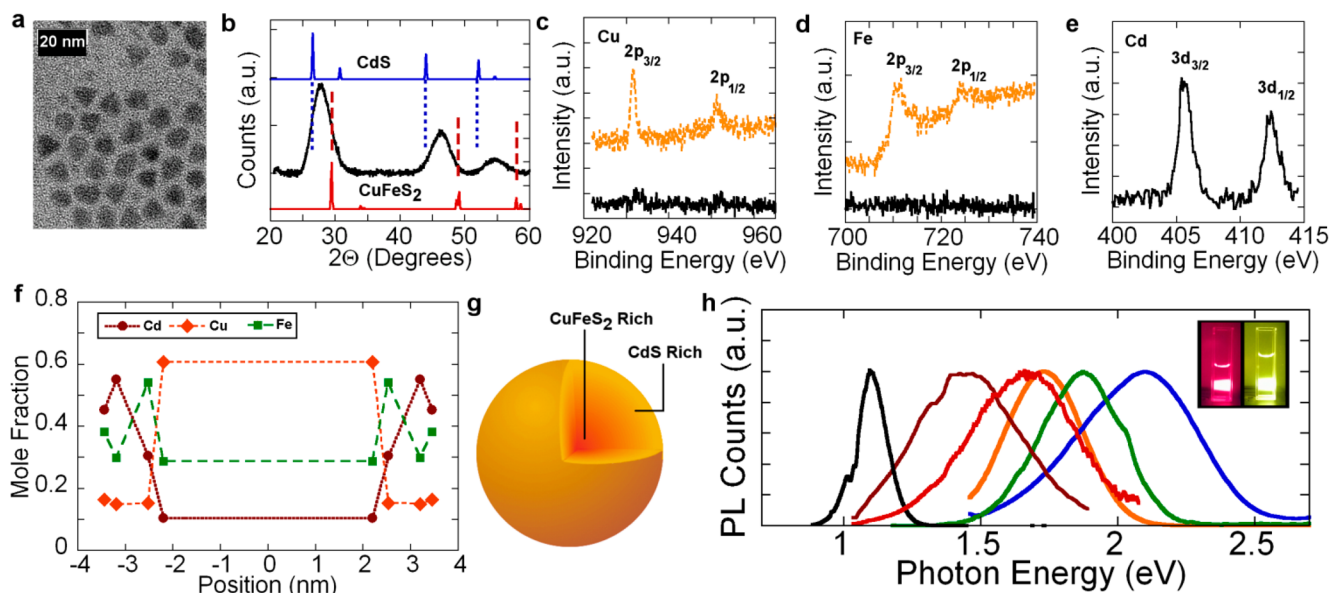
Figure 3. (a) TEM image of CuFeS$_2$/CdS QDs. (b) XRD pattern of CuFeS$_2$/CdS QDs (black). The standard patterns of CuFeS$_2$ (red, bottom) and CdS (blue, top) are also shown. (c) XPS spectra of the copper edge of CuFeS$_2$ (orange, dashed) and CuFeS$_2$/CdS QDs (black). (d) XPS spectra of the iron edge of CuFeS$_2$ (orange, dashed) and CuFeS$_2$/CdS QDs (black). (e) XPS spectrum of CuFeS$_2$/CdS QDs, showing the cadmium edge. (f) Variation of the ratios of cadmium (brown, circle), copper (red, diamond), and iron (green, square) across the QD profile, as revealed by layer-by-layer etching. (g) Schematic of a CuFeS$_2$/CdS QD as inferred from panels (a)−(f). (h) PL emission from CuFeS$_2$/CdS QDs. Inset: Emission from red (87% QY) and yellow (54% QY) emitting QDs.

of ∼0.35 within the effective mass approximation. Coulomb effects have been neglected in this estimate. For comparison, a semiconductor such as CdSe exhibits a value of 0.1,[42] while PbSe exhibits a much lower value of 0.03.[43]

The observed empirical size−band gap relationship for CuFeS$_2$ QDs may be written as

$$E = \frac{4.304}{d^2} + 0.515$$

or

$$d = \sqrt{\frac{4.304}{E - 0.515}}$$

Here E is the optical band gap in electronvolts of the QD as determined from a Tauc plot for a direct gap semiconductor and d is the particle diameter in nanometers determined from TEM. This expression has been verified for 3−15 nm QDs.

CORE/SHELL STRUCTURES

As-prepared CuFeS$_2$ QDs do not exhibit measurable luminescence. It is however found that the growth of a CdS shell leads to a very significant enhancement in emission. We employed the surface lability of CuFeS$_2$ particles in order to prepare core/shell structures. While as-prepared QDs are stable in their growth solutions, it was found that attempts at shell growth at high temperatures cause the etching and degradation of the entire ensemble. We therefore synthesized core/shell architectures at a much lower temperature by treating QDs with cadmium oleate. This approach is similar to the one adopted for the synthesis of lead chalcogenide core/shell architectures.

Briefly, as-prepared CuFeS$_2$ QDs were heated to 150 °C. Cadmium oleate (1 mL of a 0.1 mM solution per 2 mL of the CuFeS$_2$ original solution) was then added. Figure 3a exemplifies a typical sample of core/shell QDs prepared

through this route. The band gap of these materials is observed to be blue shifted as the reaction proceeds. We studied the compositional homogeneity of these materials using energy dispersive X-ray spectroscopy (EDX) elemental mapping with a scanning transmission electron microscope (STEM). This technique allowed for the determination of elements present on each QD, thereby demonstrating compositional homogeneity. The results of this elemental mapping technique are exemplified in the Supporting Information, Figures S2 and S3. We find that CdS growth causes the introduction of cadmium into each QD. We were also able to observe simultaneous signatures of copper, iron, and sulfur from each dot, providing direct, visual evidence of CdS growth.

The structural changes associated with CdS growth were studied using XRD. Figure 3b shows a typical pattern of CuFeS$_2$/CdS QDs (black) produced by this route. The standard patterns of CdS and CuFeS$_2$ are indicated by blue and red curves, respectively. The lack of a clear CdS or CuFeS$_2$ pattern in these materials as well as the intermediate position of the resulting pattern implies alloy formation in terms of Vegard's law.[44] While Vegard's law allows for the estimation of alloy composition, it nevertheless represents only an averaged picture. Local structural inhomogeneities are not observable via this technique. In order to further examine the precise effects of the CdS shell, we studied the surfaces of these QDs using X-ray photoelectron spectroscopy (XPS). The photoelectron spectra obtained from pure CuFeS$_2$ QDs are shown in Figure 3c,d (yellow, dashed lines). XPS therefore shows the presence of both cations on the surface of as-prepared CuFeS$_2$ QDs.[45] The core/shell growth procedure leads to the disappearance of Cu and Fe lines from XPS spectra (Figure 3c,d, black lines) along with the appearance of Cd lines (Figure 3e). XPS analysis thus indicates the formation of a CdS overlayer on CuFeS$_2$ QDs through the shell growth procedure.[46]

In order to understand the nature of the $CuFeS_2$–CdS alloy that is suggested by XRD, we examined the composition profile of $CuFeS_2$/CdS QDs by slow digestion. $CuFeS_2$/CdS QDs were separated from the reaction mixture by treatment with alcohols. The QDs were then treated with dilute (2 N) nitric acid to induce slow etching. The etched ions were then quantitatively transferred into a volumetric flask. The ratios as well as the total moles of ions removed by this procedure were determined through inductively coupled plasma optical emission spectroscopy (ICP-OES).

This procedure enables a layer-by-layer reconstruction of these QDs. This is shown in Figure 3f. We find that the outer layers indeed contain larger amounts of cadmium, while the inner layers contain increasing amounts of copper. Apart from its absence from the surface (inferred from XPS), the mole fraction of iron does not change significantly through the QD. Instead, the cadmium treatment largely replaces copper ions in the shell region. At the same time, the inner core (~2.0 nm in this case), remains $CuFeS_2$-like. These results are qualitatively summarized in Figure 3g. It is important to note that the first step of the digestion procedure removes 20% of the $CuFeS_2$/CdS QD. The data points at ±3.7 nm thus represent an averaged composition of the outer layers of the QD, rather than just the surface composition. The existence of a composition gradient across the QD is nonetheless apparent, with the surface being cadmium rich and copper deficient, while the core region is copper rich. Despite this composition gradient, the overall volume averaged copper to iron ratio for the entire QD is observed to be 1:0.9, consistent with its interpretation as a $CuFeS_2$/CdS graded alloy core/shell.

◼ LUMINESCENCE

Besides its structural implications, treatment with cadmium and sulfur precursors leads to the appearance of a strong emission from these materials. The emission band red shifts as the QD size is increased; for example, a 5.4 nm QD is found to exhibit emission at 1.59 eV, while a smaller 3 nm QD has an emission maximum at 1.65 eV. The size dependence of the emission implies the involvement of quantum confined levels in the emission process; however, the full extent of their role still needs to be elucidated. Figure 3h exemplifies the emission spectra of $CuFeS_2$/CdS QDs. These materials are highly emissive over the 0.7–2.5 eV window, with the highest observed quantum yields (QYs) as high as 87% at 1.87 eV. It is further noteworthy that $CuFeS_2$/CdS QDs that are tuned to the visible wavelengths have remarkably small sizes, e.g. 2.4 nm in this particular example. The inset to Figure 3h exemplifies bright visible luminescence from $CuFeS_2$/CdS core/shell structures. Besides their high QYs, $CuFeS_2$/CdS QDs also exhibit a broad emission bandwidth with a full width at half-maximum (fwhm) as broad as 0.48 eV over the range of samples studied in this work.

Regardless of the broad emission line width as well as the lack of distinct features in the absorption spectrum, we find that the $CuFeS_2$/CdS band edge is associated with a surprisingly sharp bleach feature. The transient absorption dynamics of these QDs was studied by illuminating the QD sample with a 400 nm, 100 fs pulse derived from a Coherent Libra amplified laser. The bleach spectrum for a population of <0.1 exciton per QD was obtained by probing the sample with a broadband femtosecond probe. Figure 4a shows the transient bleach spectrum of the QD sample (green dots) 3 ps after the arrival of the pump. Despite the relatively broad emission line width
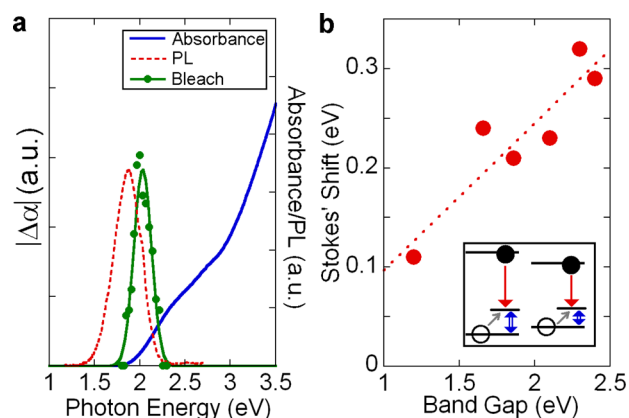

Figure 4. (a) Absorbance, photoluminescence (PL), and transient pump induced changes in absorbance ($\Delta\alpha$) in $CuFeS_2$/CdS QDs. (b) Variation of Stokes shift of $CuFeS_2$/CdS QDs as a function of their band edge 1S feature position. Inset: Schematic of the defect based mechanism for origin of Stokes shift. The red arrow represents a radiative transition from the conduction band to a defect level. The gray arrow represents nonradiative relaxation, and the blue double arrows represent the Stokes shift. The QD on the left is smaller in size and has greater confinement than the QD on the right.

(0.34 eV, dashed red curve), the bleach feature that is observed after complete electronic cooling exhibits a narrower line width of 0.21 eV (solid green curve). The existence of a strong long-lived bleach implies the persistence of electrons at the QD band edge. At the same time, the significantly different widths of the absorption and emission features are indicative of a significantly phonon coupled emission, such as expected from a defect state. A defect based emission mechanism is also accepted as the explanation of the properties of other copper based ternaries such as $CuInS_2$.[47,48] Since the valence band of copper based I–III–VI$_2$ ternaries is known to be derived from copper and chalcogenide atoms, the existence of a similar family of copper related defects in $CuFeS_2$ is very likely.[49] We find that the optical properties of $CuFeS_2$/CdS QDs are indeed consistent with such an interpretation.

For example, it is further apparent that the emission maximum is significantly Stokes shifted relative to the bleach feature. In the example shown in Figure 4a, the emission is 0.16 eV red shifted relative to the bleach feature, and 0.23 eV relative to the lowest excitonic feature (at 2.1 eV on the blue curve). We further note that the Stokes shift of $CuFeS_2$/CdS QDs decreases for large QDs (Figure 4b). We observe a linear increase of the Stokes shift with increasing QD band gap energy. Within a defect emission picture,[50] the Stokes shift originates from the differences in energy of the quantum confined energy levels that are responsible for optical absorption and the defect levels. This is shown in the inset to Figure 4b. Emission involves an electron at the conduction band edge and a hole localized at the defect center.[47,51] We note that the presence of the electron at the conduction band edge is confirmed from our observation of a strong optical pump induced bleach feature.[47] The Stokes shift (double blue arrows in Figure 4b, inset) thus arises because of the presence of a valence band defect within the band gap.[52] With increasing QD size, quantum confinement decreases and the quantum confined valence band level approaches the defect level. This leads to a corresponding decrease in the Stokes shift. The data follow a linear trend (dashed line, Figure 4b) that is expected from such a description. Extrapolating this line to the bulk band

gap of the material allows us to estimate the energy of the defect relative to the $CuFeS_2$ bulk valence band. We estimate a Stokes shift of 0.03 eV for a QD band edge at 0.52 eV, thereby implying that the defect is ∼0.03 eV below the $CuFeS_2$ bulk valence band edge.

A model that involves a delocalized conduction band electron along with a valence band hole localized at an internal defect thus completely explains all steady state characteristics of $CuFeS_2$/CdS QD emission. We further note that the lack of emission in core-only $CuFeS_2$ QDs is consistent with the nonradiative decay at surface defects. This is discussed further in the Supporting Information, Figure S4.

The variation of Stokes shift with QD band gap is accompanied by a corresponding change in the emission decay kinetics. In general, it is observed that sample lifetimes increase with decreasing band edge energies. Figure 5a shows
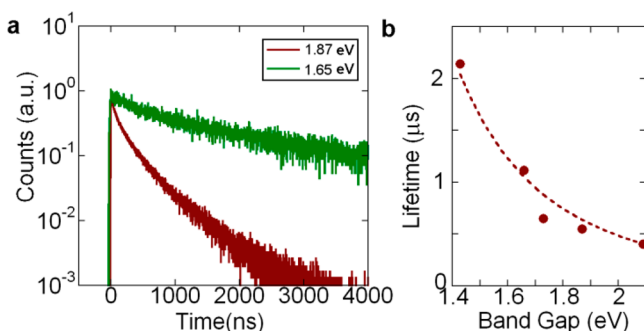

Figure 5. (a) Emission kinetics of samples with band edges at 1.87 eV (brown) and 1.65 eV (green). (b) Variation of emission lifetime with band gap (emission maximum). The dashed line is a fit described in text.

the emission kinetics observed for two different $CuFeS_2$/CdS samples. The samples decay with average lifetimes of 503 ns (brown) and 1117 ns (green), corresponding to the emission maxima of 1.87 and 1.65 eV, respectively. The decay kinetics has been measured at the peak of the sample emission in each case. Emission lifetimes increase by nearly an order of magnitude as the emission maximum is shifted from 2.2 to 1.4 eV (Figure 5b). The data closely follow a $(E - E_g)^{-3}$ curve (dashed line) that is expected for emission from a defective system.[51] This relationship is expected based on arguments of defect−quantum confined level overlap. The overlap of a quantum confined level with a defect scales inversely with the QD volume. The confinement energy $(E - E_g)$ itself scales as $V^{-2/3}$, where V is the QD volume. Finally, the lifetime itself is proportional to the inverse square of the overlap, leading to the $(E - E_g)^{-3}$ dependence on confinement energy. As shown in Figure 5b, this trend is accurately describes the evolution of sample kinetics, confirming the involvement of a valence band defect.

We further studied inhomogeneities in the emission kinetics of $CuFeS_2$/CdS QDs. As shown in Figure 6a, the emission profile of a single batch of QDs evolves in time, shifting increasingly toward redder wavelengths following the initial photoexcitation. Such inhomogeneities have been previously observed in $CuInS_2$ QDs and have been taken to imply the existence of defect centers with different characteristic properties.[53,54] In the context of $CuFeS_2$/CdS, this inhomogeneity is significantly small in magnitude, and is consistent with the existence of defects with slightly different overlaps with the
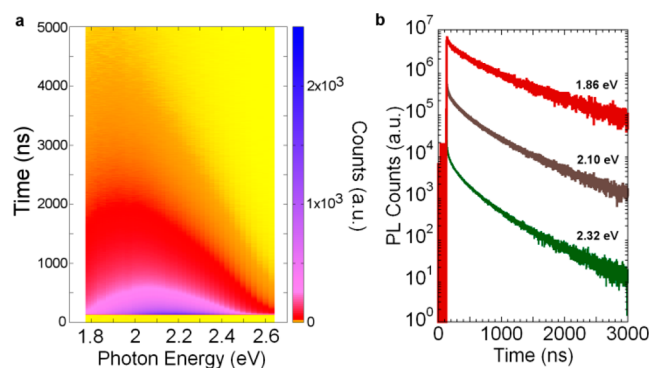

Figure 6. (a) Two-dimensional plot of decay kinetics of a $CuFeS_2$/CdS sample. (b) Decay traces at the peak (2.1 eV) and fwhm's (1.86 and 2.32 eV) of the emission. Decay traces have been offset for clarity.

conduction band quantum confined levels.[55] This is expected from a graded alloy structure that gives rise to copper centers with varying local environments. It is important to note that this inhomogeneity, exemplified in Figure 6a, is actually fairly small and does not affect our interpretation of Figure 5. For example, Figure 6b shows the decay kinetics of the emission maximum (2.10 eV) as well as the half-maximum positions of the emission band (1.86 and 2.32 eV). We observe average lifetimes of 411 ns at 1.86 eV, 403 ns at 2.10 eV, and 386 ns at 2.32 eV. The variation of lifetimes across a band is thus clearly small compared to the variation of lifetimes across different samples. At the same time, this variation of lifetimes does lead to a systematic red shift of the emission maximum at longer times. We thus find that all structural and optical properties of $CuFeS_2$ QDs can be consistently explained by a valence band defect based emission picture, described in the inset to Figure 4b[56] and Figure S4 in the Supporting Information.

■ CROSS SECTIONS

The strong luminescence of $CuFeS_2$ based QDs as well as their large size tunability suggests a vast potential in optoelectronics. In particular, $CuFeS_2$ based QDs could possibly replace II−VI and III−V materials in the visible to near-infrared region in certain cases. In order to explore its potential in this spectroscopic region further, we examined the optical absorption cross sections of $CuFeS_2$ QDs. We find that $CuFeS_2$ is a strong light absorber, making it quite interesting for a range of optical and optoelectronic applications. Figure 7 shows the volume normalized optical cross section of a 4 nm sample of $CuFeS_2$ QDs. Volume normalized cross sections between 10^3 and 10^4 cm^{-1} are observed in the 1−1.5 eV region,
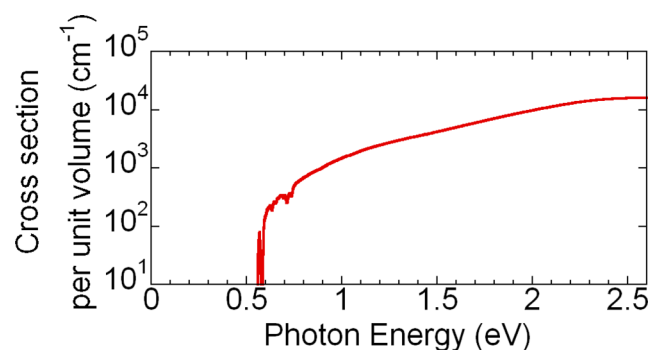

Figure 7. Cross section per unit volume of a $CuFeS_2$ QD.

which are comparable to those observed for II−VI materials such as CdTe.[57,58] CuFeS$_2$ QDs further exhibit absorption cross sections of $5.3 \times 10^{-17}a^3$ cm^2 at 400 nm. Here a is the particle radius in nanometers. This corresponds to a molar extinction coefficient of $1.39 \times 10^4 a^3$ M^{-1} cm^{-1} at the same wavelength. For comparison, copper indium sulfide QDs exhibit a cross section of $1.8 \times 10^{-16}a^3$ at the same wavelength.[47]

CONCLUSIONS

In conclusion, we demonstrate the synthesis of CuFeS$_2$ QDs and their core/shell structures. CuFeS$_2$ based core/shell architectures are seen to exhibit very high PL QYs that can exceed 80% in some cases. Additionally, CuFeS$_2$ based QDs that are emissive over the visible region have extremely small sizes. These QDs exhibit long, band gap dependent excitonic lifetimes that increase by almost an order of magnitude as the band gap of the QDs is increased. These materials also exhibit a strong Stokes shift that can be as large as 0.3 eV for smaller QDs. Finally, these materials are extremely stable under ambient conditions (Figures S5 and S6 of the Supporting Information). This suggests applications of these materials as phosphors and luminescent concentrators. We interpret their emissive properties in terms of a valence band defect located 30 meV below the bulk valence band edge. The overall emission characteristics of this material bear strong similarities to those of copper indium sulfide, suggesting a common origin to the emission mechanism of both materials.

CuFeS$_2$ QDs are shown to exhibit a tunable band gap energy that may be varied over the entire near-infrared region as well as the red edge of the visible spectrum. The large cross sections per unit volume of these materials suggest uses in a host of optical and optoelectronic applications. CuFeS$_2$ QDs are to date the only size tunable infrared band gap QD that contains only lighter (atomic number 30 or less) elements.

ASSOCIATED CONTENT

Ⓢ Supporting Information

The Supporting Information is available free of charge on the ACS Publications website at DOI: 10.1021/jacs.6b04981.

> Details of synthetic and characterization procedure (PDF)

AUTHOR INFORMATION

Corresponding Author
*anshup@sscu.iisc.ernet.in.

Notes
The authors declare no competing financial interest.

ACKNOWLEDGMENTS

REFERENCES

(1) Kamat, P. V. J. Phys. Chem. Lett. **2013**, 4, 908−918.
(2) Carey, G. H.; Abdelhady, A. L.; Ning, Z.; Thon, S. M.; Bakr, O. M.; Sargent, E. H. Chem. Rev. **2015**, 115, 12732−12763.
(3) Keuleyan, S.; Lhuillier, E.; Brajuskovic, V.; Guyot-Sionnest, P. Nat. Photonics **2011**, 5, 489−493.
(4) Medintz, I. L.; Uyeda, H. T.; Goldman, E. R.; Mattoussi, H. Nat. Mater. **2005**, 4, 435−446.
(5) Pietryga, J. M.; Schaller, R. D.; Werder, D.; Stewart, M. H.; Klimov, V. I.; Hollingsworth, J. A. J. Am. Chem. Soc. **2004**, 126, 11752−11753.
(6) Kim, S.; Marshall, A. R.; Kroupa, D. M.; Miller, E. M.; Luther, J. M.; Jeong, S.; Beard, M. C. ACS Nano **2015**, 9, 8157−8164.
(7) Zhang, J.; Gao, J.; Miller, E. M.; Luther, J. M.; Beard, M. C. ACS Nano **2014**, 8, 614−622.
(8) Peng, Z. A.; Peng, X. J. Am. Chem. Soc. **2001**, 123, 183−184.
(9) Shen, H.; Wang, H.; Chen, X.; Niu, J. Z.; Xu, W.; Li, X. M.; Jiang, X. D.; Du, Z.; Li, L. S. Chem. Mater. **2010**, 22, 4756−4761.
(10) Kamal, J. S.; Omari, A.; Van Hoecke, K.; Zhao, Q.; Vantomme, A.; Vanhaecke, F.; Capek, R. K.; Hens, Z. J. Phys. Chem. C **2012**, 116, 5049−5054.
(11) McDaniel, H.; Zuo, J. M.; Shim, M. J. Am. Chem. Soc. **2010**, 132, 3286−3288.
(12) Flanagan, J. C.; Shim, M. J. Phys. Chem. C **2015**, 119, 20162−20168.
(13) Guo, S.; Fidler, A. F.; He, K.; Su, D.; Chen, G.; Lin, Q.; Pietryga, J. M.; Klimov, V. I. J. Am. Chem. Soc. **2015**, 137, 15074−15077.
(14) Kovalenko, M. V.; Heiss, W.; Shevchenko, E. V.; Lee, J. S.; Schwinghammer, H.; Alivisatos, A. P.; Talapin, D. V. J. Am. Chem. Soc. **2007**, 129, 11354−11355.
(15) Liu, W.; Chang, A. Y.; Schaller, R. D.; Talapin, D. V. J. Am. Chem. Soc. **2012**, 134, 20258−20261.
(16) Zimmer, J. P.; Kim, S. W.; Ohnishi, S.; Tanaka, E.; Frangioni, J. V.; Bawendi, M. G. J. Am. Chem. Soc. **2006**, 128, 2526−2527.
(17) Kovalenko, M. V.; Kaufmann, E.; Pachinger, D.; Roither, J.; Huber, M.; Stangl, J.; Hesser, G.; Schäffler, F.; Heiss, W. J. Am. Chem. Soc. **2006**, 128, 3516−3517.
(18) Zhang, W. H.; Yang, J.; Yu, J. S. J. Mater. Chem. **2012**, 22, 6383−6388.
(19) Keuleyan, S.; Lhuillier, E.; Guyot-Sionnest, P. J. Am. Chem. Soc. **2011**, 133, 16422−16424.
(20) Allen, P. M.; Bawendi, M. G. J. Am. Chem. Soc. **2008**, 130, 9240−9241.
(21) Panthani, M. G.; Akhavan, V.; Goodfellow, B.; Schmidtke, J. P.; Dunn, L.; Dodabalapur, A.; Barbara, P. F.; Korgel, B. A. J. Am. Chem. Soc. **2008**, 130, 16770−16777.
(22) Regulacio, M. D.; Han, M.-Y. Acc. Chem. Res. **2016**, 49, 511−519.
(23) Kim, J. Y.; Yang, J.; Yu, J. H.; Baek, W.; Lee, C. H.; Son, H. J.; Hyeon, T.; Ko, M. J. ACS Nano **2015**, 9, 11286−11295.
(24) Holman, Z. C.; Kortshagen, U. R. Nano Lett. **2011**, 11, 2133−2136.
(25) Dayeh, S. A.; Wang, J.; Li, N.; Huang, J. Y.; Gin, A. V.; Picraux, S. T. Nano Lett. **2011**, 11, 4200−4206.
(26) Zhao, J. Y.; Chen, G.; Gu, Y. P.; Cui, R.; Zhang, Z. L.; Yu, Z. L.; Tang, B.; Zhao, Y. F.; Pang, D. W. J. Am. Chem. Soc. **2016**, 138, 1893−1903.
(27) Zhu, C. N.; Jiang, P.; Zhang, Z. L.; Zhu, D. L.; Tian, Z. Q.; Pang, D. W. ACS Appl. Mater. Interfaces **2013**, 5, 1186−1189.
(28) Zhuang, Z.; Peng, Q.; Zhang, B.; Li, Y. J. Am. Chem. Soc. **2008**, 130, 10482−10483.
(29) Wong, A. B.; Brittman, S.; Yu, Y.; Dasgupta, N. P.; Yang, P. Nano Lett. **2015**, 15, 4096−4101.
(30) Wu, Y.; Wadia, C.; Ma, W.; Sadtler, B.; Alivisatos, A. P. Nano Lett. **2008**, 8, 2551−2555.
(31) Puthussery, J.; Seefeld, S.; Berry, N.; Gibbs, M.; Law, M. J. Am. Chem. Soc. **2011**, 133, 716−719.
(32) Bai, Y.; Yeom, J.; Yang, M.; Cha, S. H.; Sun, K.; Kotov, N. A. J. Phys. Chem. C **2013**, 117, 2567−2573.
(33) Babayigit, A.; Duy Thanh, D.; Ethirajan, A.; Manca, J.; Muller, M.; Boyen, H. G.; Conings, B. Sci. Rep. **2016**, 6, 18721.
(34) Khan, S.; Hesham, A. E. L.; Qiao, M.; Rehman, S.; He, J. Z. Environ. Sci. Pollut. Res. **2010**, 17, 288−296.
(35) Babayigit, A.; Ethirajan, A.; Muller, M.; Conings, B. Nat. Mater. **2016**, 15, 247−251.

(36) Kambara, T. *J. Phys. Soc. Jpn.* **1974**, *36*, 1625−1635.

(37) Liang, D.; Ma, R.; Jiao, S.; Pang, G.; Feng, S. *Nanoscale* **2012**, *4*, 6265−6268.

(38) Conejeros, S.; Alemany, P.; Llunell, M.; Moreira, I. P. R.; Sánchez, V.; Llanos, J. *Inorg. Chem.* **2015**, *54*, 4840−4849.

(39) Ang, R.; Khan, A. U.; Tsujii, N.; Takai, K.; Nakamura, R.; Mori, T. *Angew. Chem., Int. Ed.* **2015**, *54*, 12909−12913.

(40) Hamajima, T.; Kambara, T.; Gondaira, K. I.; Oguchi, T. *Phys. Rev. B: Condens. Matter Mater. Phys.* **1981**, *24*, 3349−3353.

(41) Fujisawa, M.; Suga, S.; Mizokawa, T.; Fujimori, A.; Sato, K. *Phys. Rev. B: Condens. Matter Mater. Phys.* **1994**, *49*, 7155−7164.

(42) Norris, D. J.; Bawendi, M. G. *Phys. Rev. B: Condens. Matter Mater. Phys.* **1996**, *53*, 16338−16346.

(43) Martinez, G.; Schlüter, M.; Cohen, M. L. *Phys. Rev. B* **1975**, *11*, 651−659.

(44) Mukherjee, S.; Nag, A.; Kocevski, V.; Santra, P. K.; Balasubramanian, M.; Chattopadhyay, S.; Shibata, T.; Schaefers, F.; Rusz, J.; Gerard, C.; Eriksson, O.; Segre, C. U.; Sarma, D. D. *Phys. Rev. B: Condens. Matter Mater. Phys.* **2014**, *89*, 224105.

(45) Velásquez, P.; Leinen, D.; Pascual, J.; Ramos-Barrado, J. R.; Grez, P.; Gómez, H.; Schrebler, R.; Del Río, R.; Córdova, R. *J. Phys. Chem. B* **2005**, *109*, 4977−4988.

(46) Nanda, J.; Kuruvilla, B. A.; Sarma, D. D. *Phys. Rev. B: Condens. Matter Mater. Phys.* **1999**, *59*, 7473−7479.

(47) Li, L.; Pandey, A.; Werder, D. J.; Khanal, B. P.; Pietryga, J. M.; Klimov, V. I. *J. Am. Chem. Soc.* **2011**, *133*, 1176−1179.

(48) Zhong, H.; Lo, S. S.; Mirkovic, T.; Li, Y.; Ding, Y.; Li, Y.; Scholes, G. D. *ACS Nano* **2010**, *4*, 5253−5262.

(49) Jaffe, J. E.; Zunger, A. *Phys. Rev. B: Condens. Matter Mater. Phys.* **1984**, *29*, 1882−1906.

(50) Kolny-Olesiak, J.; Weller, H. *ACS Appl. Mater. Interfaces* **2013**, *5*, 12221−12237.

(51) Jara, D. H.; Stamplecoskie, K. G.; Kamat, P. V. *J. Phys. Chem. Lett.* **2016**, *7*, 1452−1459.

(52) Azimi, H.; Heumüller, T.; Gerl, A.; Matt, G.; Kubis, P.; Distaso, M.; Ahmad, R.; Akdas, T.; Richter, M.; Peukert, W.; Brabec, C. J. *Adv. Energy Mater.* **2013**, *3*, 1589−1596.

(53) Song, W. S.; Yang, H. *Chem. Mater.* **2012**, *24*, 1961−1967.

(54) Kim, Y. K.; Ahn, S. H.; Chung, K.; Cho, Y. S.; Choi, C. J. *J. Mater. Chem.* **2012**, *22*, 1516−1520.

(55) Ozaki, S.; Muto, K. I.; Nagata, H.; Adachi, S. *J. Appl. Phys.* **2005**, *97*, 043507.

(56) Zhang, S. B.; Wei, S. H.; Zunger, A.; Katayama-Yoshida, H. *Phys. Rev. B: Condens. Matter Mater. Phys.* **1998**, *57*, 9642−9656.

(57) Mitchell, K.; Fahrenbruch, A. L.; Bube, R. H. *J. Appl. Phys.* **1977**, *48*, 829−830.

(58) Mahadevu, R.; Yelameli, A. R.; Panigrahy, B.; Pandey, A. *ACS Nano* **2013**, *7*, 11055−11063.